



Crack tip fields at a ductile single crystal-rigid material interface

A. NAKATANI¹, W. J. DRUGAN², E. VAN DER GIESSEN³ and A. NEEDLEMAN⁴

¹*Osaka University, Department of Adaptive Machine Systems, Yamadaoka, Suita, Osaka 565-0871, Japan (e-mail: nakatani@ams.eng.osaka-u.ac.jp)*

²*University of Wisconsin, Department of Engineering Physics, Madison, WI 53706, U.S.A. (e-mail: drugan@engr.wisc.edu)*

³*University of Groningen, Department of Applied Physics, Nyenborgh 4, 9747 AG Groningen, The Netherlands (e-mail: Giessen@phys.rug.nl)*

⁴*Brown University, Division of Engineering, Providence, RI 02912, U.S.A. (e-mail: needle@engin.brown.edu)*

Received 22 May 2002; accepted in revised form 5 September 2003

Abstract. Small-scale yielding around a stationary crack along a ductile single crystal–rigid material interface is analyzed. Plane strain conditions are assumed to prevail and geometry changes are neglected. The analyses are carried out using both continuum slip and discrete dislocation plasticity theory for model fcc and bcc crystal geometries having either two or three slip systems. Numerical and analytical asymptotic solutions are presented for continuum slip plasticity theory. Solutions exhibiting both slip bands and kink bands are obtained. The addition of a third slip system to ductile single crystals having two slip systems is found to have a significant effect on the interface crack-tip fields. The results illustrate the role that each of the formulations considered can play in elucidating crack tip fields in single crystals.

Key words: Crack tip plasticity, crystal plasticity, dislocations, fracture mechanisms.

1. Introduction

Metal-ceramic interfaces are found in a variety of components and structures, and fracture at or near such interfaces often limits reliability. Knowledge of the stress and deformation fields at the crack tip at a single crystal-ceramic interface is needed in order to develop a fundamental understanding of this fracture process. For homogeneous single crystals, crack tip stress and deformation fields have been analyzed using continuum slip plasticity theory, analytically, e.g. by Rice (1987) and Drugan (2001), and computationally, e.g. by Rice et al. (1990) and Cuitiño and Ortiz (1993), and using discrete dislocation plasticity, e.g. by Cleveringa et al. (2000) and Van der Giessen et al. (2001). Each of these analysis frameworks has advantages and disadvantages in elucidating crack tip fields in crystalline solids.

Analytical solutions explicitly reveal the parameter dependence of the near-tip fields and provide closed-form expressions for the stress fields and key deformation field features, but are asymptotic in nature, with an unspecified region of dominance, and are restricted to infinitesimal deformations, thus neglecting effects of crack blunting and lattice rotations. The asymptotic solutions show that the discreteness of slip systems gives rise to near-tip stress and deformation fields that differ substantially from the corresponding fields for isotropic solids, Rice (1987), Saeedvafa and Rice (1989), Drugan (2001). In particular, in the non-hardening limit (Rice, 1987; Drugan, 2001), the near-tip stress fields in yielded regions consist solely of sectors of constant Cartesian components of stress. In Rice's (1987) solutions the sector boundaries are associated with either a slip band (slip direction along the band) or a kink band

(slip direction perpendicular to the band), and all of his solutions require the presence of both slip and kink bands. The non-hardening plasticity solutions are not unique and Drugan (2001) has obtained solutions that only involve localized slip bands.

Finite element solutions based on continuum slip plasticity, as in Rice et al. (1990) and Cuitiño and Ortiz (1993), provide full-field solutions and can account for finite deformation effects. However, the very sharp gradients characteristic of near crack tip deformation fields are difficult to reproduce in finite element solutions. In addition, extracting the parameter dependence of the fields requires extensive parameter studies that are computationally time consuming. This is especially important for non-hardening or lightly hardening crystals where the non-uniqueness of the asymptotic fields suggests a strong sensitivity of crack tip fields to details of the formulation. In addition, as is also true for the analytical solutions, the presumption underlying such numerical calculations is that conventional continuum slip plasticity appropriately characterizes the material response in the near crack tip region.

The discrete dislocation calculations of Cleveringa et al. (2000) and Van der Giessen et al. (2001) are even more time consuming than the continuum slip finite element solutions and, for computational reasons, are confined to small regions near the crack tip. However, the discrete dislocation calculations reveal the dual role played by the dislocations. On the one hand, the dissipation associated with dislocation motion gives rise to a toughness much higher than that associated with the work of creating new surface. On the other hand, the local stress concentration associated with discrete dislocation patterning leads to near-tip stress levels much higher than predicted by conventional continuum plasticity, which is key for precipitating fracture.

In this paper, we investigate crack tip stress and deformation fields at metal-ceramic interfaces using analytical, finite element and discrete dislocation approaches. Attention is focused on small scale yielding of stationary cracks in plane strain, with the ceramic idealized as rigid. Also, geometry changes are neglected in all calculations. The predicted crack tip fields obtained from the three frameworks are compared. An issue in multi-scale modeling is the consistency between the predictions of different formulations; in particular, the appropriate matching of models that pertain at smaller and larger length scales. Comparisons of the predictions of different models, as in the present study, can provide information to improve modeling at each of the scales considered.

2. Problem formulation

A crack along a metal-ceramic interface is considered, with the ceramic idealized as rigid. The elastic properties of the metal are taken to be isotropic, with Young's modulus E and Poisson's ratio ν . Small scale yielding conditions are considered. Attention is confined to small strains, plane strain conditions are assumed to prevail and a Cartesian coordinate system is used with the x_1 - x_2 plane being the plane of deformation.

The boundary value problem is sketched in Figure 1a. In complex variable notation, the elastic singular stress fields along the interface, near the tip of an interfacial crack at $(x_1, x_2) = (0, 0)$ have the form (England, 1965; Erdogan, 1965; Rice and Sih, 1965; Rice, 1988),

$$\sigma_{22} + i\sigma_{12} = \frac{K}{\sqrt{2\pi x_1}}(x_1)^{i\epsilon}, \quad i = \sqrt{-1} \quad (1)$$

with

$$K = K_1 + iK_2, \quad \epsilon = \frac{1}{2\pi} \ln \left(\frac{1 - \beta}{1 + \beta} \right). \quad (2)$$

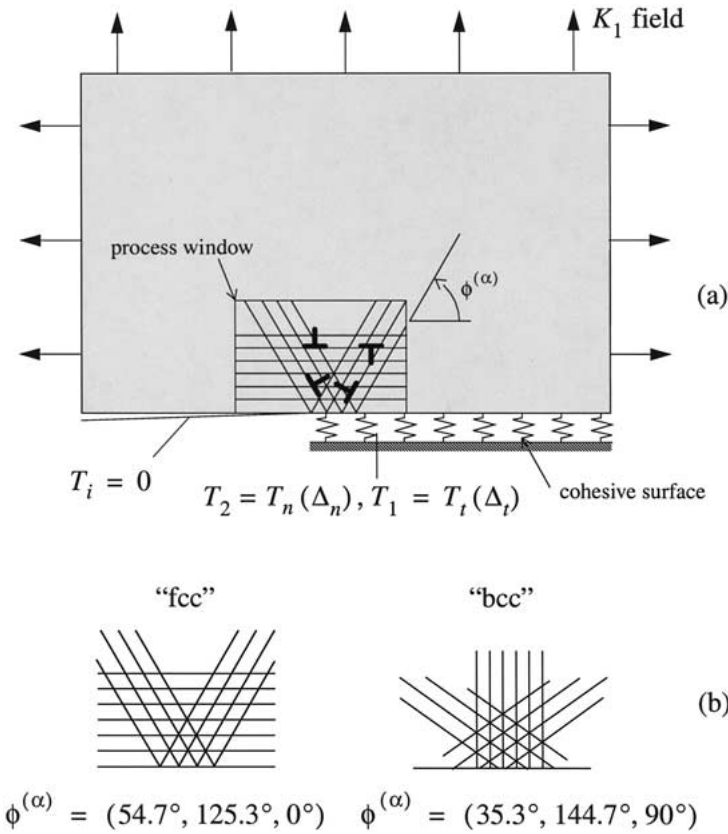


Figure 1. (a) Small scale yielding analysis for a plastically deforming solid on a rigid substrate. (b) Crystal geometries analyzed.

K_1 and K_2 are the mode I and mode II stress intensity factors, respectively. The oscillatory index ϵ is expressed in terms of one of the Dundurs (1969) parameters, β , which for an elastic-rigid material system simplifies to

$$\beta = -\frac{1(1-2\nu)}{2(1-\nu)}; \quad (3)$$

the other Dundurs parameter $\alpha = -1$ in this case.

Interfacial crack tip fields differ from those for homogeneous materials in several significant respects, Rice (1988), Shih (1991), Hutchinson and Suo (1992). First, near-tip interface crack tip fields are mixed mode, involving both tension (mode I) and shear (mode II), for purely tensile remote loading. The ratio of shear to normal traction ahead of the crack-tip varies with distance from the tip due to the oscillatory nature of the singularity. Furthermore, the normal traction on the bond line becomes compressive in the vicinity of the crack tip, implying that contact occurs. The extent of the contact region and how close it is to the crack tip depend on the value of ϵ defined in (2) and on the remote loading.

The small-scale yielding boundary conditions involve imposing displacements corresponding to the elastic singular field for an interface crack on the remote boundaries. The displacements $u = u_1 + iu_2$ corresponding to (1) are prescribed at the remote boundary and are given by

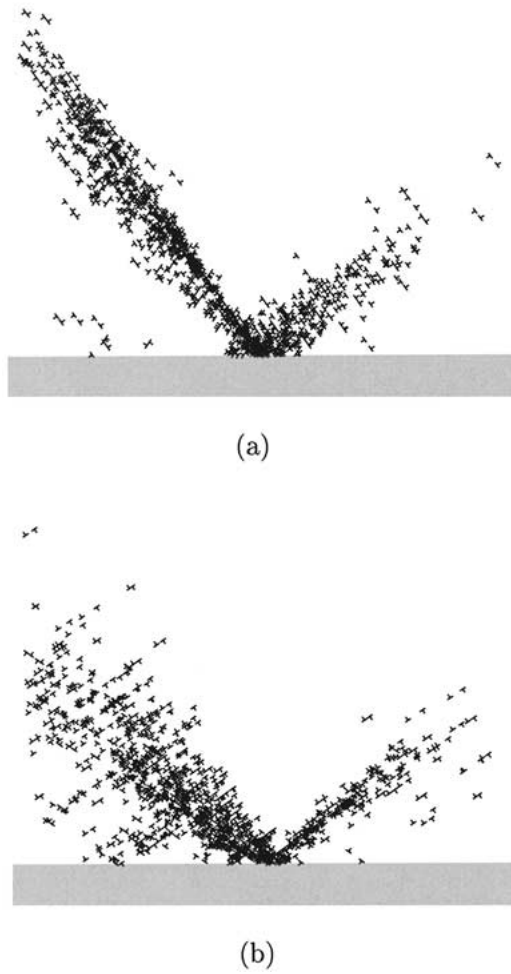


Figure 2. Dislocation configurations for the two-slip-system calculations at $K_1/K_0 = 0.717$. The size of the region shown is $24 \times 24 \mu\text{m}$. (a) fcc type crystal geometry. (b) bcc type crystal geometry.

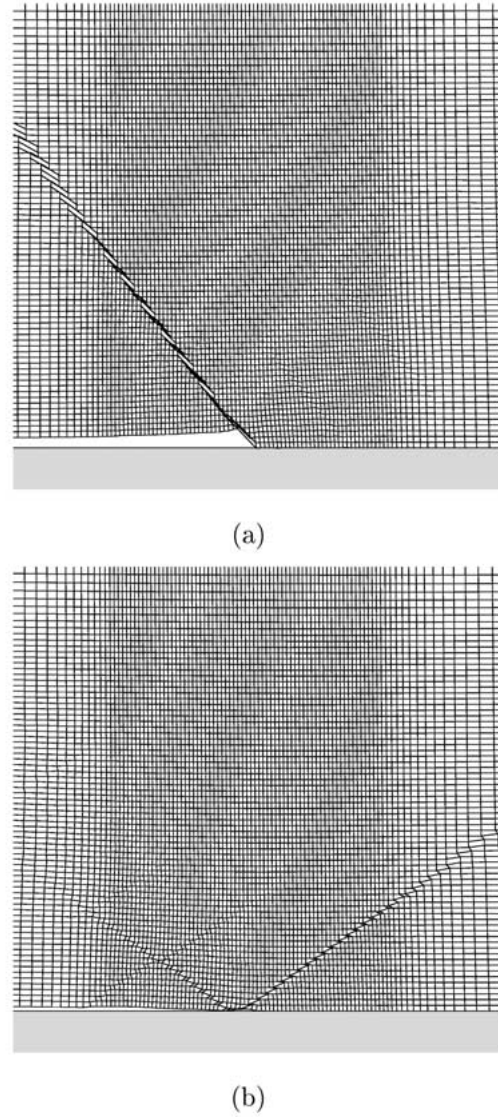


Figure 3. Deformed meshes for the two-slip-system calculations at $K_1/K_0 = 0.717$. The size of the region shown is $6 \times 6 \mu\text{m}$. (a) fcc type crystal geometry. (b) bcc type crystal geometry.

$$u = \frac{2(1+\nu)}{E} \frac{|K|r^{1/2}}{2\sqrt{2\pi} \cosh(\pi\epsilon)} \left[\frac{(3-4\nu) \exp(\bar{\theta}-i\bar{\psi}) - \exp(-\bar{\theta}-i\bar{\psi})}{1-2i\epsilon} - i \sin \theta \exp(\bar{\theta}+i\bar{\psi}) \right] \quad (4)$$

where

$$r = \sqrt{x_1^2 + x_2^2}, \quad \theta = \tan^{-1}(x_2/x_1), \quad (5)$$

$$\bar{\theta} = \frac{i\theta}{2} + \epsilon(\theta - \pi), \quad \bar{\psi} = \psi + \epsilon \ln\left(\frac{r}{L}\right), \quad (6)$$

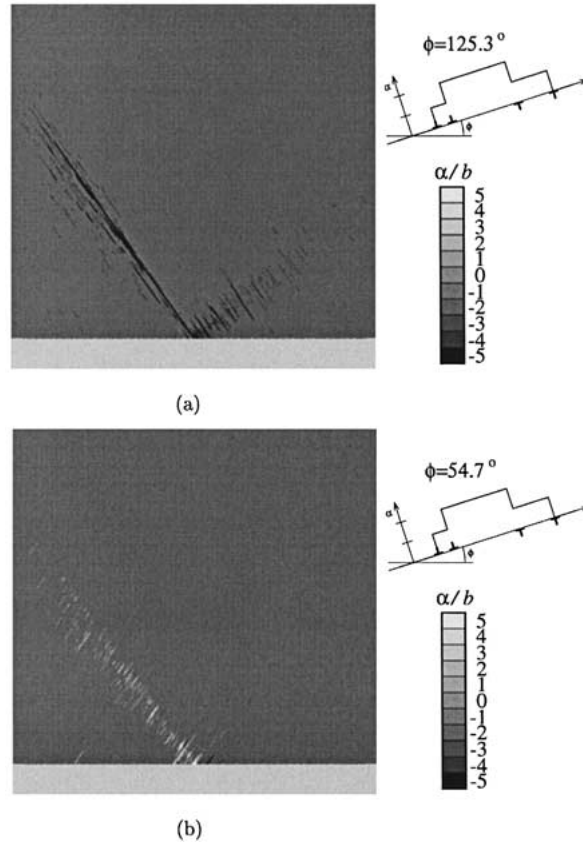


Figure 4. Slip distribution for the two-slip-system fcc type crystal geometry at $K_1/K_0 = 0.717$. The size of the region shown is $24 \times 24 \mu\text{m}$. (a) $\phi^{(2)} = 125.3^\circ$. (b) $\phi^{(1)} = 54.7^\circ$.

with

$$\tan \psi = \frac{\Im [KL^{i\epsilon}]}{\Re [KL^{i\epsilon}]} \quad (7)$$

and L a reference length. Here $\Re[\cdot]$ and $\Im[\cdot]$ denote, respectively, the real and imaginary parts of a complex quantity.

Since the initial crack is at the origin,

$$\sigma_{12}(x_1, 0) = \sigma_{22}(x_1, 0) = 0 \quad \text{for } x_1 < 0. \quad (8)$$

The continuum slip calculations, both analytical and finite element, are carried out for a perfect bond between the crystal and the rigid substrate, so that

$$u_1(x_1, 0) = u_2(x_1, 0) = 0 \quad \text{for } x_1 > 0. \quad (9)$$

3. Discrete dislocation plasticity

In the discrete dislocation calculations, plastic flow is confined to a small region near the current crack tip (termed ‘process window’ in Figure 1) and takes place by the nucleation and

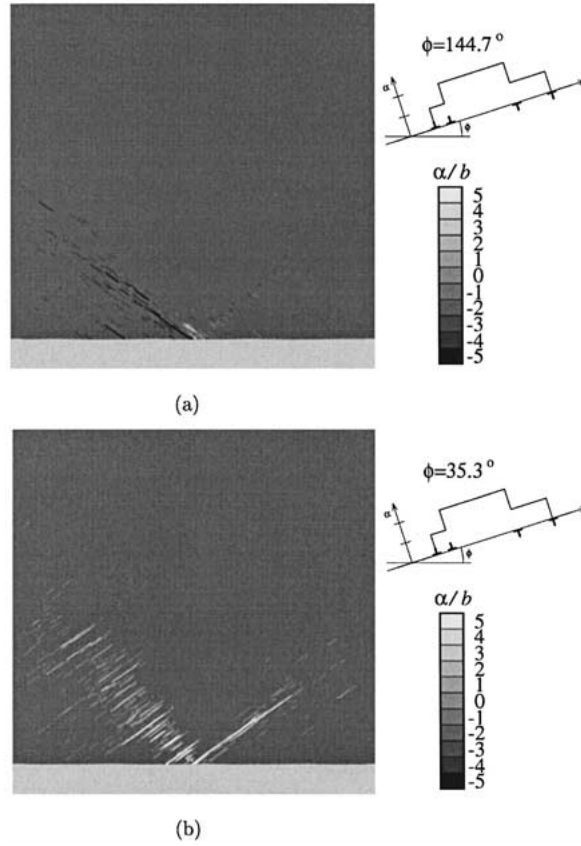


Figure 5. Slip distribution for the two-slip-system bcc type crystal geometry at $K_1/K_0 = 0.717$. The size of the region shown is $24 \times 24 \mu\text{m}$. (a) $\phi^{(2)} = 144.7^\circ$. (b) $\phi^{(1)} = 35.3^\circ$.

glide of discrete dislocations, which are treated as line singularities. Also, although attention is restricted to stationary cracks, the calculations are carried out with a cohesive surface specified along $x_2 = 0$ for $x_1 > 0$ (Figure 1a) which is taken to have the mixed-mode form given in Xu and Needleman (1993). However, the remote loading is restricted to small enough amplitudes for the opening of the cohesive surface to be negligible so that the boundary condition (9) is satisfied approximately. Nevertheless, the work of separation of the cohesive surface, ϕ_n , does provide a convenient quantity for normalizing the amplitude of the remote stress intensity factor, namely through the reference intensity factor

$$K_0 = \sqrt{\frac{E\phi_n}{1-\nu^2}}. \quad (10)$$

3.1. COMPUTATIONAL METHOD

The computation of the deformation history is carried out in an incremental manner with a monotonically increasing value of K_1 prescribed in (4) and with $K_2 \equiv 0$. At each time increment, we calculate (i) the updated dislocation structure and (ii) the rate of change of all fields. For the latter, we separate out the singular part of the dislocation fields by writing the velocity, strain-rate and stress-rate fields as the superposition of two fields,

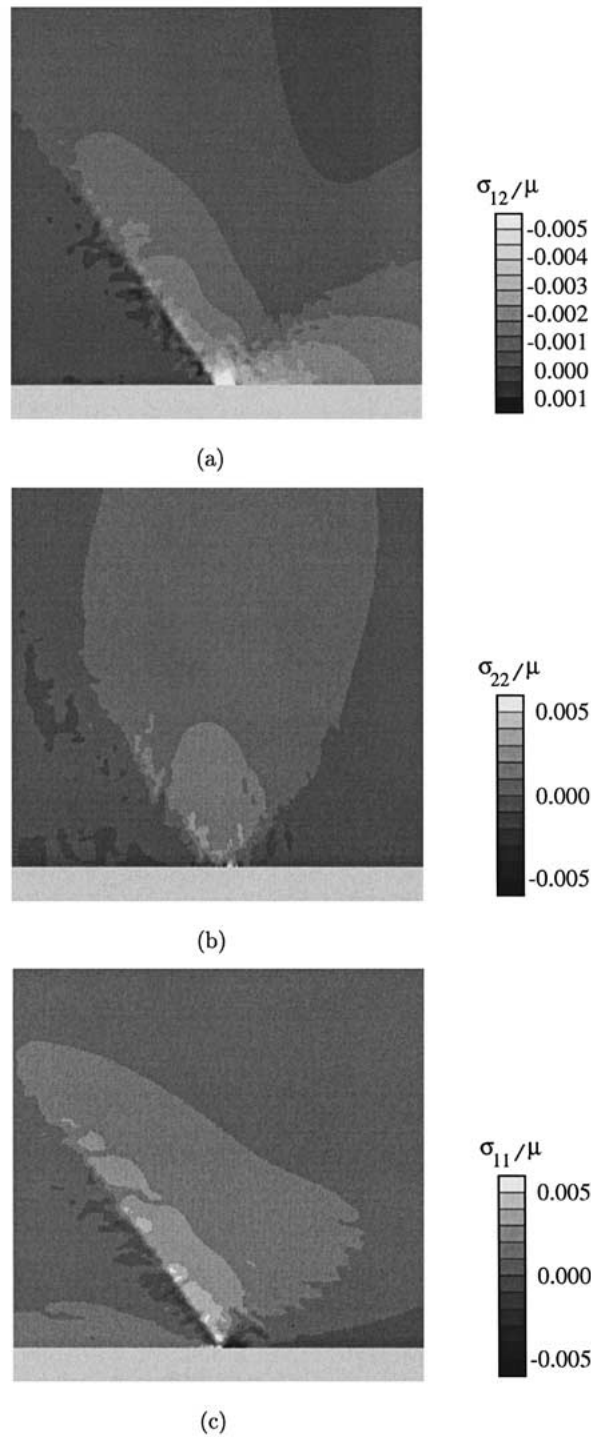


Figure 6. Contours of stress components for the two-slip-system fcc type crystal geometry at $K_1/K_0 = 0.717$. The size of the region shown is $24 \times 24 \mu\text{m}$. (a) σ_{12} . (b) σ_{22} . (c) σ_{11} .

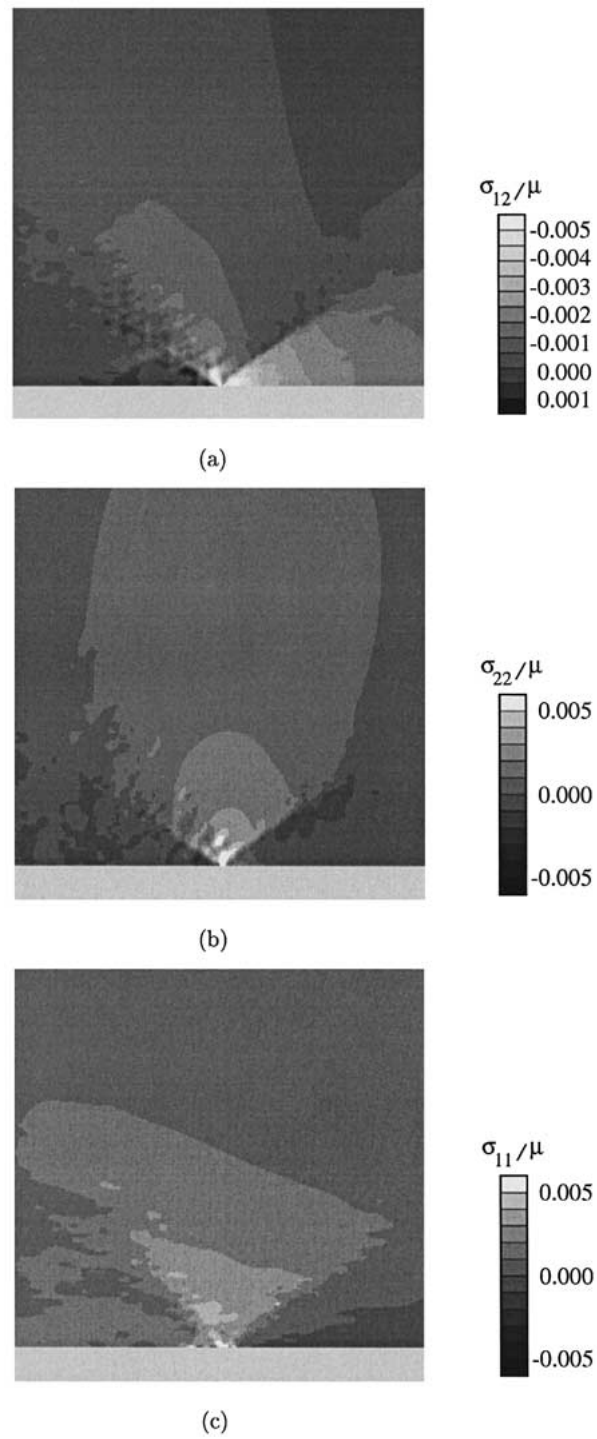
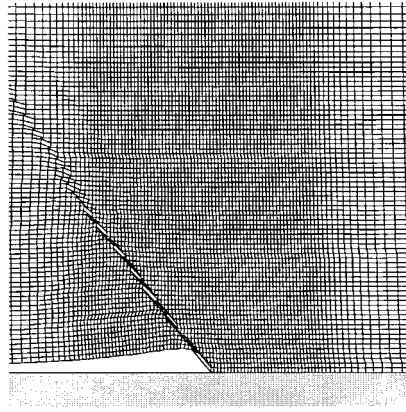
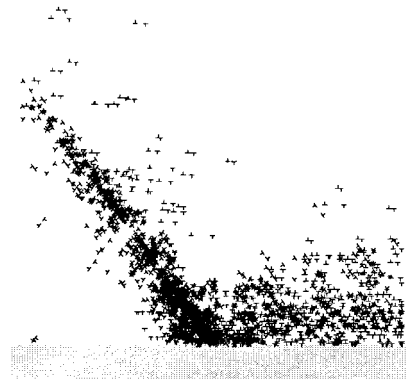


Figure 7. Contours of stress components for the two-slip-system bcc type crystal geometry at $K_1/K_0 = 0.717$. The size of the region shown is $24 \times 24 \mu\text{m}$. (a) σ_{12} . (b) σ_{22} . (c) σ_{11} .



(a)



(b)

Figure 8. (a) Deformed mesh for the three-slip-system fcc calculation at $K_1/K_0 = 0.717$. The size of the region shown is $6 \times 6 \mu\text{m}$. (b) Dislocation configuration for the three-slip-system fcc calculation at $K_1/K_0 = 0.717$. The size of the region shown is $24 \times 24 \mu\text{m}$.

$$\dot{u}_i = \tilde{u}_i + \hat{u}_i, \quad \dot{\epsilon}_{ij} = \tilde{\epsilon}_{ij} + \hat{\epsilon}_{ij}, \quad \dot{\sigma}_{ij} = \tilde{\sigma}_{ij} + \hat{\sigma}_{ij}. \quad (11)$$

The $(\hat{\cdot})$ fields are the fields of the individual dislocations, in their current configuration but in infinite space, which differs from the formulation in Cleveringa et al. (2000) where half-space dislocation fields were used. The $(\tilde{\cdot})$ fields correct for the actual boundary conditions and are obtained with a finite element method; see Cleveringa et al. (2000) for details.

All dislocations are purely edge, with their line direction normal to the x_1 - x_2 plane and with the same magnitude b of their Burgers vector. With the stress field and the current positions of all dislocations known at time t , the dislocation glide, the generation of new dislocations, their mutual annihilation, and their possible pinning at obstacles within the increment Δt is determined. The same constitutive rules are used for these events as in Cleveringa et al. (2000). The magnitude of the glide velocity $v^{(I)}$ of dislocation I is taken to be linearly related to the Peach–Koehler force $f^{(I)}$ through the drag relation

$$f^{(I)} = Bv^{(I)}, \quad (12)$$

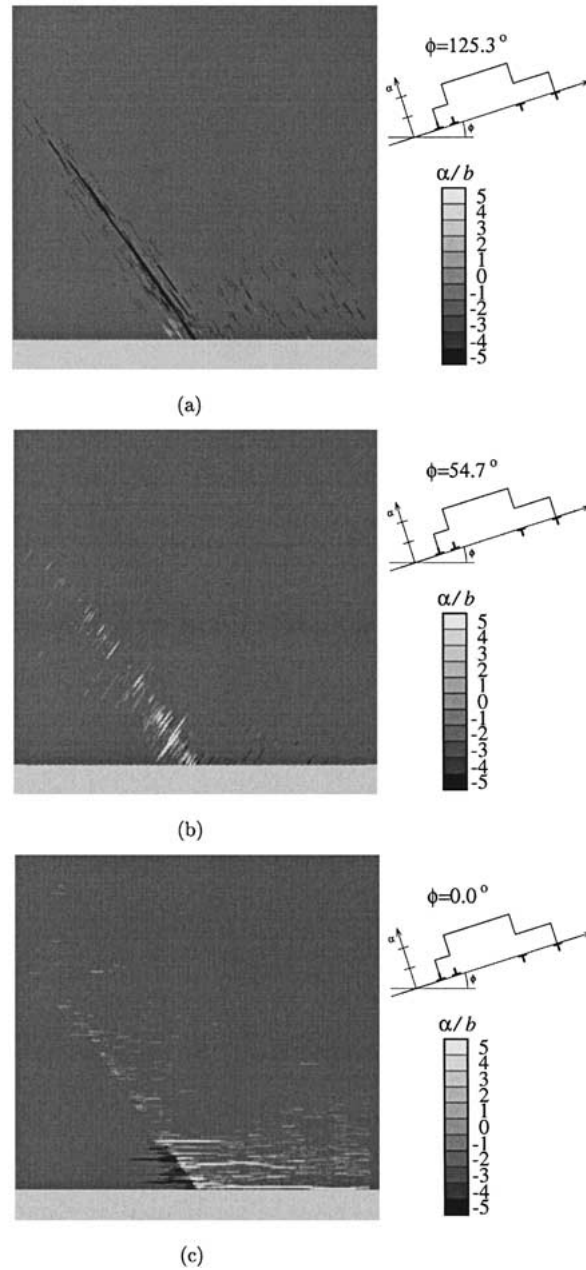


Figure 9. Slip distribution for the three-slip-system fcc type crystal geometry at $K_1/K_0 = 0.717$. The size of the region shown is $24 \times 24 \mu\text{m}$. (a) $\phi^{(2)} = 125.3^\circ$. (b) $\phi^{(1)} = 54.7^\circ$. (c) $\phi^{(3)} = 0^\circ$.

where B is the drag coefficient. The Peach–Koehler force is calculated from the stress state by

$$f^{(I)} = N_i^{(I)} \left(\hat{\sigma}_{ij} + \sum_{J \neq I} \sigma_{ij}^{(J)} \right) b_j^{(I)}, \quad (13)$$

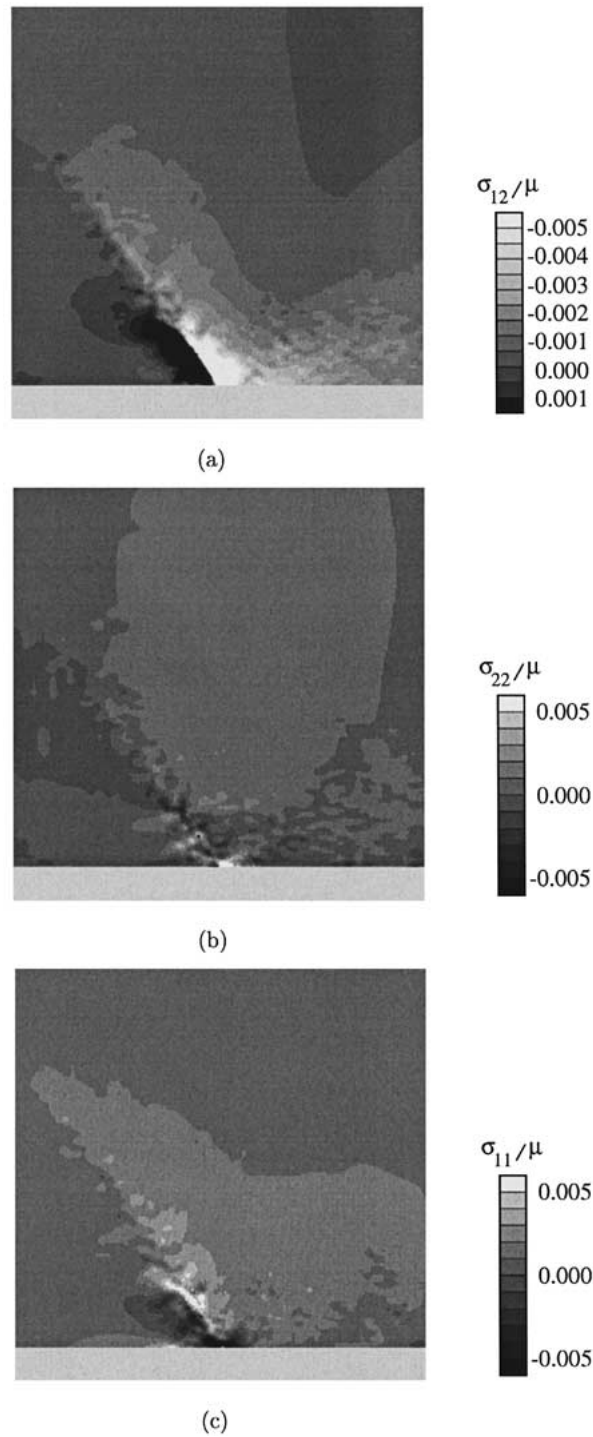


Figure 10. Stress contours for the three-slip-system fcc calculation at $K_1/K_0 = 0.717$. The size of the region shown is $24 \times 24 \mu\text{m}$. (a) σ_{12} . (b) σ_{22} . (c) σ_{11} .

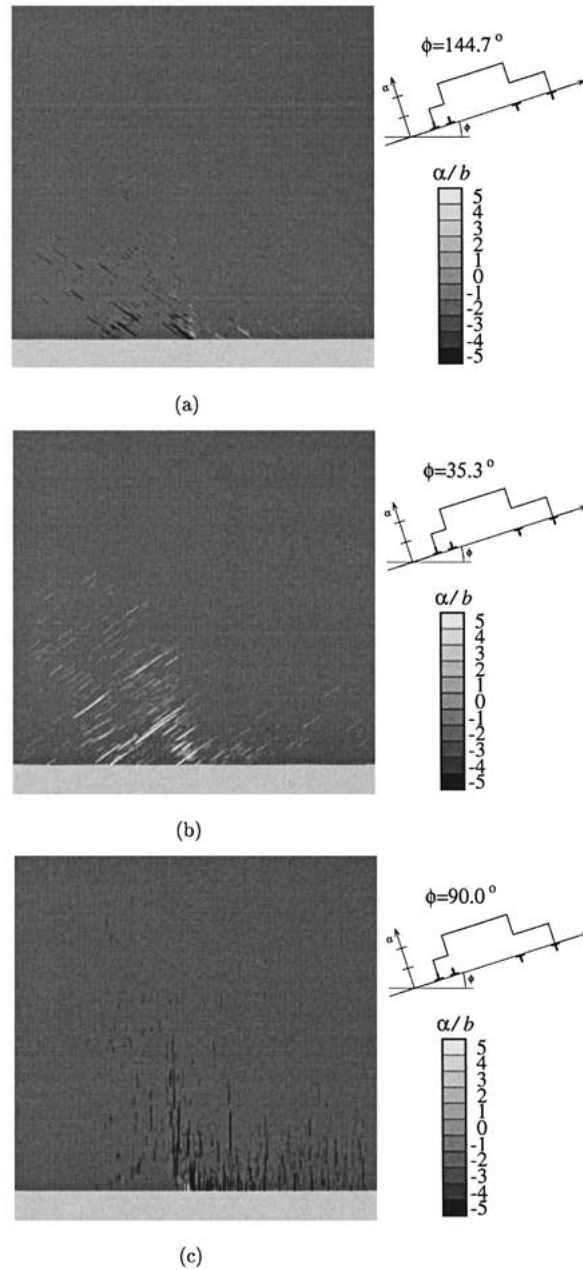


Figure 11. Slip distribution for the three-slip-system bcc type crystal geometry at $K_1/K_0 = 0.717$. The size of the region shown is $24 \times 24 \mu\text{m}$. (a) $\phi^{(2)} = 144.7^\circ$. (b) $\phi^{(1)} = 35.3^\circ$. (c) $\phi^{(3)} = 90^\circ$.

with $N_i^{(I)}$ the slip plane normal and $b_i^{(I)}$ the Burgers vector of dislocation I . The generation of new dislocations by a Frank-Read mechanism is simulated in two dimensions through point sources which generate a dislocation dipole when the magnitude of the Peach–Koehler force at the source exceeds a critical value $\tau_{\text{nuc}}b$ during a period of time t_{nuc} . The strength of the dislocation sources is randomly chosen from a Gaussian distribution with mean strength $\bar{\tau}_{\text{nuc}}$ and standard deviation $0.2\bar{\tau}_{\text{nuc}}$. Annihilation of two dislocations with opposite Burgers

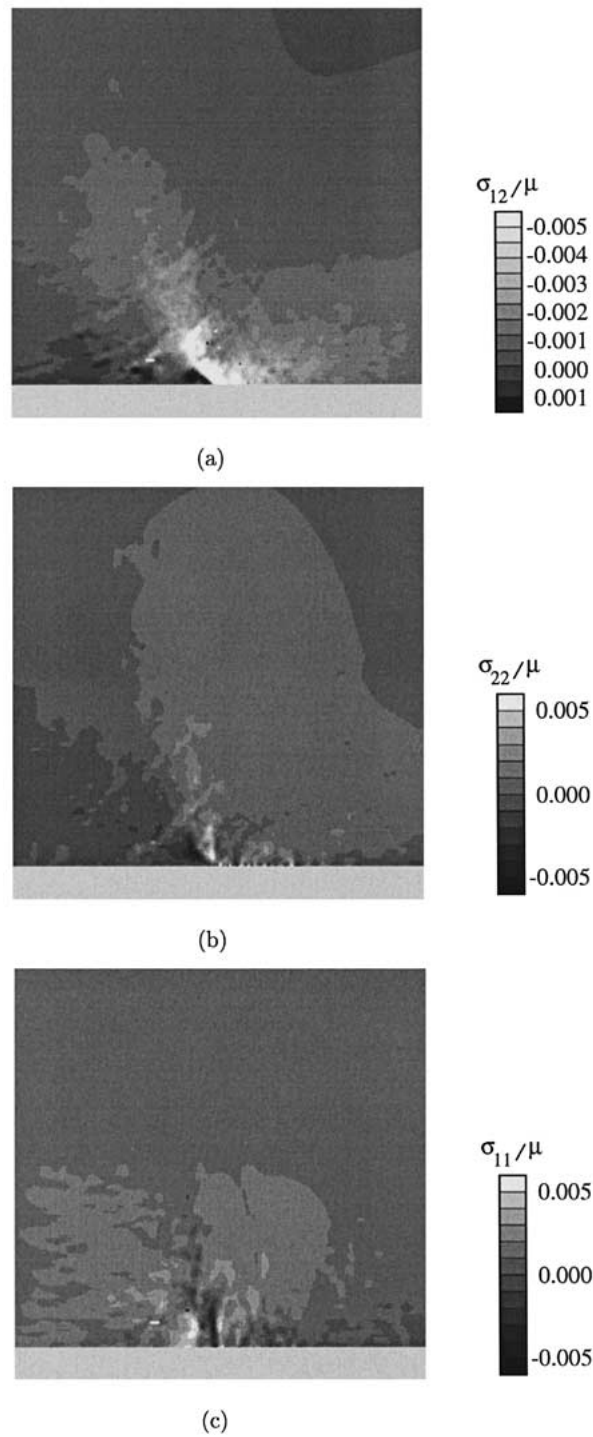


Figure 12. Stress contours for the three-slip-system bcc calculation at $K_1/K_0 = 0.717$. The size of the region shown is $24 \times 24 \mu\text{m}$. (a) σ_{12} . (b) σ_{22} . (c) σ_{11} .

vectors occurs when they are sufficiently close together, i.e. within the annihilation distance $L_e = 6b$. Obstacles to dislocation motion are modeled as fixed points on a slip plane. Pinned dislocations can only pass an obstacle when its Peach-Koehler force exceeds an obstacle-dependent value $\tau_{\text{obs}}b$.

In tension, these constitutive rules give rise to a tensile stress–strain curve that is essentially ideally plastic, with a yield strength on the order of the mean nucleation stress τ_{nuc} , see for example Deshpande et al. (2003). However, the hardness depends on the dislocation structure; strain gradients in the vicinity of the crack induce dislocation structures with a net Burgers vector (geometrically necessary dislocations) that give rise to increased hardening. This hardening is a nonlocal effect that is not accounted for by conventional, local continuum slip plasticity theory.

3.2. NUMERICAL RESULTS

Results will be presented for parameter values that are representative for aluminum as the metal phase. The elastic properties of the crystal are approximated as being isotropic, with $E = 70$ GPa and $\nu = 0.33$, giving a shear modulus μ of 26.3 GPa. The magnitude of the Burgers vector b is specified to have the value 0.25 nm. Calculations are carried out for two crystal geometries with two slip systems and two crystal geometries with three slip systems as sketched in Figure 1b. For one three-slip-system geometry, the slip planes make angles $\phi^{(\alpha)} = (54.7^\circ, 125.3^\circ, 0^\circ)$ with the x_1 -axis; for the other three-slip-system geometry $\phi^{(\alpha)} = (35.3^\circ, 144.7^\circ, 90^\circ)$. These correspond, respectively, to the fcc and bcc type geometries of Rice (1987). The two-slip-system geometries are obtained by removing the slip systems parallel to the coordinate axes so that $\phi^{(\alpha)} = (54.7^\circ, 125.3^\circ)$ for the fcc type crystal geometry and $\phi^{(\alpha)} = (35.3^\circ, 144.7^\circ)$ for the bcc type crystal geometry. In all cases, the slip plane spacing is $0.1 \mu\text{m}$, i.e. $400b$. The drag coefficient has the value $B = 10^{-4}\text{Pa s}$ and the mean nucleation strength is $\bar{\tau}_{\text{nuc}} = 50$ MPa. The nucleation time is $t_{\text{nuc}} = 0.01 \mu\text{s}$ for all sources. The strength of all randomly placed obstacles is $\tau_{\text{obs}} = 150$ MPa.

The displacement boundary conditions (4) are imposed on a semi-circle of radius $R = 0.02$ m. A finite element mesh of 19348 bilinear quadrilateral elements is used, with a square grid inside the process window. Plastic deformation is confined to a process window which is taken to have dimensions $L_p = 22.5 \mu\text{m}$ by $H_p = 32.5 \mu\text{m}$. The mesh in the process window consists of 132×134 rectangular elements with a refined uniform mesh of 64×64 elements in a region of $3.2 \mu\text{m}$ by $4.53 \mu\text{m}$ in the vicinity of the crack tip. In this region, the size of each element is $0.05 \times 0.0707 \mu\text{m}$. All results in this section are for the prescribed K_1 having the value $K_1/K_0 = 0.717$, with K_0 defined by (10).

3.2.1. Two slip systems

Figure 2 shows the dislocation distributions obtained for the two-slip-system fcc (Figure 2a) and bcc (Figure 2b) type crystal geometries. The dislocations occur primarily in two bands aligned with the two slip planes emanating from the crack tip. For the bcc type crystal geometry, there is considerable dislocation activity between $\theta = 144.7^\circ$ and the crack flank.

The near-tip deformation fields associated with these dislocation structures are shown by the deformed mesh plots in Figure 3. For the fcc type crystal geometry in Figure 3a, deformation is mainly concentrated in a slip band aligned with the slip system with $\phi^{(2)} = 125.3^\circ$ which tends to blunt the crack. The dislocations ahead of the crack in Figure 2a are also mainly on the slip system at 125.3° but do not give rise to localized shearing. On the other

hand, for the bcc material in Figure 3b, slip bands associated with both the $\phi^{(1)} = 35.3^\circ$ and $\phi^{(2)} = 144.7^\circ$ slip systems are visible and the crack does not blunt.

Insight into the mode of plastic deformation is obtained by plotting the slip activity on each slip plane. In Figure 4, for the fcc type crystal geometry, and in Figure 5, for the bcc type crystal geometry, the amount of slip is denoted by α and, for each slip plane, is defined as the accumulated signed Burgers vector, with the convention for zero slip defined in the insets of Figures 4 and 5. In Figure 4a, where $\phi^{(2)} = 125.3^\circ$, slip mainly occurs in a kink type mode across the deformation band ahead of the crack tip, and in a slip type mode along the deformation band behind the crack tip. Figure 4b shows that the main deformation involving the $\phi^{(1)} = 54.7^\circ$ slip system is a kink deformation mode behind the crack tip. However, although Figure 4 shows that slip occurs on both slip systems for the band behind the crack tip in Figure 3a, this band is mainly a slip band. Figure 3a also shows that large deformations do not accumulate in the band ahead of the crack tip, whereas substantial slip deformation does accumulate in the band behind the crack tip.

Slip plots are shown in Figure 5 for the bcc type crystal geometry. Here, slip bands are seen on the $\phi^{(2)} = 144.7^\circ$ slip system behind the crack in Figure 5a and on the $\phi^{(1)} = 35.3^\circ$ slip system ahead of the crack in Figure 5b. These slip concentrations are consistent with the deformed mesh plot in Figure 3b. In addition, slip in a kink type band on the $\phi^{(1)} = 35.3^\circ$ slip system is seen. There is also a sufficient concentration of deformation in the direction of the $\phi^{(1)} = 35.3^\circ$ slip system to lead to the intense deformation in this direction behind the crack tip in Figure 3b. The orientations of the slip band in Figure 5a and the kink band in Figure 5b that are present behind the crack tip are distinctly different.

Stress distributions are shown in Figure 6 for the fcc type crystal geometry. There is a sharp gradient in σ_{12} across the slip band direction in Figure 6a. A similar sharp variation in σ_{11} is seen in Figure 6c across the slip band direction. In contrast, the contours of σ_{22} in Figure 6b show the highest values above the crack tip with a similar variation ahead of and behind the crack tip.

The stress distributions in Figure 7 are for the bcc type crystal geometry. There are relatively sharp gradients in σ_{12} , Figure 7a, and σ_{22} , Figure 7b, across the direction of the shear bands (see Figure 3b) ahead of and behind the crack tip. On the other hand, a sharp gradient in σ_{11} behind the crack tip is more aligned with the kink band direction than with the shear band direction (see Figure 5a). As for the fcc type crystal geometry, the highest opening stresses are directly above the crack tip in Figure 7b.

3.2.2. Three slip systems

The effect of a third slip system is shown Figures 8–12. The deformation pattern in Figure 8a for the three-slip-system fcc crystal is very similar to that for the two-slip-system fcc crystal in Figure 3a. The dislocation pattern in Figure 8b is, however, different from that for the two-slip-system crystal in Figure 2a. The well-defined band of dislocations on the $\phi^{(2)} = 125.3^\circ$ slip system at roughly 35° observed in Figure 2a no longer appears.

Slip plots for the three-slip-system fcc type crystal geometry are shown in Figure 9. The slip band on the $\phi^{(2)} = 125.3^\circ$ slip system behind the crack tip is consistent with the intense band of deformation in Figure 8a. The main activity on the $\phi^{(1)} = 54.7^\circ$ slip system is in a kink type band essentially coinciding with the slip band. The abrupt change in sign of the slip on the $\phi^{(3)} = 0^\circ$ slip system across the shear band is shown in Figure 9c. The dominant deformation band is not changed by the presence of the third slip system, but ahead of the crack tip there is considerable activity on the $\phi^{(3)} = 0^\circ$ slip system.

Stress distributions are shown in Figure 10. The shear stress distribution for the three-slip-system fcc type crystal geometry in Figure 10a shows the change in sign of σ_{12} across the deformation band. There is also a sharp gradient in σ_{11} across the band, Figure 10c. On the other hand, there is no sharp gradient in the opening stress σ_{22} , Figure 10b, across the band. This is similar to the stress distributions for the two-slip-system fcc crystal (see Figure 6).

Figures 11 and 12 show slip and stress distributions for a three-slip-system crystal with the bcc type crystal geometry. There is slip behind the crack tip in Figure 11b in a kink type mode for the $\phi^{(1)} = 35.3^\circ$ slip system. In Figure 12a, there are sharp gradients in σ_{12} across the slip band associated with the $\phi^{(2)} = 144.7^\circ$ system behind the crack, while the slip band perpendicular to the crack plane is associated with a sharp gradient in σ_{11} , Figure 12c. In Figure 12b, a relatively high gradient in σ_{22} is in the direction of the kink type deformation mode for the $\phi^{(1)} = 35.3^\circ$ slip system, but it is not as well-defined as that for the two-slip-system bcc crystal (see Figure 10b).

4. Continuum slip plasticity

4.1. MATERIAL MODEL

For comparison purposes, calculations are carried out in plane strain using continuum slip plasticity to describe the material response. Overviews of the continuum slip formulation and its physical background are given in Asaro (1983), Cuitiño and Ortiz (1993) and Bassani (1994).

In the continuum slip calculations, the total strain rate is written as the sum of an elastic part, $\dot{\epsilon}_{ij}^e = L_{ijkl}^{-1} \dot{\sigma}_{ij}$, with L_{ijkl} the tensor of elastic moduli, and a plastic part, $\dot{\epsilon}_{ij}^p$, given by

$$\dot{\epsilon}_{ij}^p = \sum_{\alpha} \frac{\dot{\gamma}^{(\alpha)}}{2} (S_i^{(\alpha)} N_j^{(\alpha)} + S_j^{(\alpha)} N_i^{(\alpha)}), \quad (14)$$

where $S_i^{(\alpha)}$ specifies the slip direction for slip system α and $N_i^{(\alpha)}$ the slip plane normal for slip system α .

Ideal plastic behavior is assumed so that $\tau^{(\alpha)} = S_i^{(\alpha)} \sigma_{ij} N_j^{(\alpha)} = g_0$ during plastic flow, where g_0 is the planar slip system flow strength which is taken here to have the same value for all slip systems. In the numerical calculations, a small amount of rate sensitivity is introduced for stability so that the slip rate, $\dot{\gamma}^{(\alpha)}$, is taken to depend on the resolved shear stress, $\tau^{(\alpha)} = S_i^{(\alpha)} \sigma_{ij} N_j^{(\alpha)}$ via

$$\dot{\gamma}^{(\alpha)} = \dot{\gamma}_0 \left(\frac{\tau^{(\alpha)}}{g_0} \right) \left(\left| \frac{\tau^{(\alpha)}}{g_0} \right| \right)^{(1/m)-1} \quad (15)$$

with $g_0 = 30$ MPa, $m = 0.005$ and $\dot{\gamma}_0 = 0.001$ s⁻¹. Calculations were carried out using various values of g_0 and the value $g_0 = 30$ MPa was chosen because the plastic zone sizes obtained using this value give a good fit to those found in the discrete dislocation simulations.

4.2. NUMERICAL RESULTS

The elastic constants and the loading parameters are the same as used in the discrete dislocation calculations. However, in the continuum slip calculations, perfect bonding is assumed between the crystal and the rigid substrate, Equation (9), and the displacement boundary

conditions (4) are imposed on a semi-circle of radius $R = 0.01$ m. To facilitate comparison with the discrete dislocation results, dimensional lengths are used, although only relative, not absolute, values of lengths matter in the continuum calculations.

Figure 13 shows the continuum slip predictions for the two-slip-system fcc type crystal geometry. The slip and stress distributions are consistent with those seen for the corresponding discrete dislocation calculations in Figures 3a, 4a and 6a. Corresponding results for the three-slip-system fcc type crystal geometry are presented in Figure 14. These are qualitatively consistent with the discrete dislocation results in Figures 8a, 9a and 10a, although the deformation in the slip band in Figure 14a is considerably less intense than the one in Figure 8a.

4.3. ANALYTICAL SOLUTIONS

Here we employ the continuum theory of elastic-plastic single crystals to construct asymptotic analytical solutions for the metal-ceramic interface cracks. As in the discrete dislocation analyses, we shall idealize the ceramic as being rigid; the metal will be idealized as being non-hardening, and asymptotic solutions will be sought that are at yield at all angles about the crack tip on the metal side of the interface.

The methods of crack tip analysis to be employed are those of Rice (1987) and Drugan (2001). Specifically, Rice (1987) proved that the near-tip fields in yielded non-hardening single crystalline materials must be assembled from angular sectors of constant Cartesian components of stress. This is a consequence of the requirements of equilibrium and the polygonal shape of the yield surface. These uniform-stress sectors must join each other across rays having continuous traction but that may have a jump in the radial normal stress. When such a ray is aligned with a slip direction, a slip-type radial displacement jump is produced. A kink-type radial displacement jump is produced when such a ray is aligned with a normal to a slip direction. Here we will present asymptotic solutions that are in agreement with the discrete dislocation simulations and with the numerical continuum slip plasticity results. While we will explain the construction of these solutions, the reader is referred to Rice (1987) and Drugan (2001) for the mathematical details of the underlying asymptotic analysis.

The non-hardening asymptotic crack tip fields are not unique. The stress evolutions obtained from the discrete dislocation and numerical continuum slip plasticity calculations are used to guide the construction of the asymptotic solution. On the other hand, the interpretation of the stress evolution in the numerical solutions is guided by the analytical framework. To illustrate this, Figures 15d and 16d show the slip pattern assumed in the asymptotic analysis, for crystals with two and three slip systems, respectively, while Figure 17 shows the stress space evolution of the sector-averaged stress states from the numerical continuum slip solutions (Figure 18 shows a similar plot for discrete dislocation results). The two-slip-system and three-slip-system yield surfaces are also shown. Obviously, Figures 17 and 18 could not have been made without knowing the sector structure.

4.3.1. Two slip systems

We first analyze the two crystal geometries having two slip systems, as illustrated in Figure 15. The physical plane is shown in Figures 15a and 15b, for the fcc and bcc cases, respectively; note that the two available slip systems illustrated here are rotated by 90° relative to one another. It is convenient in the analyses to take the positive sense of the slip directions, $S_i^{(\alpha)}$, and the slip plane normals, $N_i^{(\alpha)}$, as indicated in Figure 15, which is not necessarily consistent

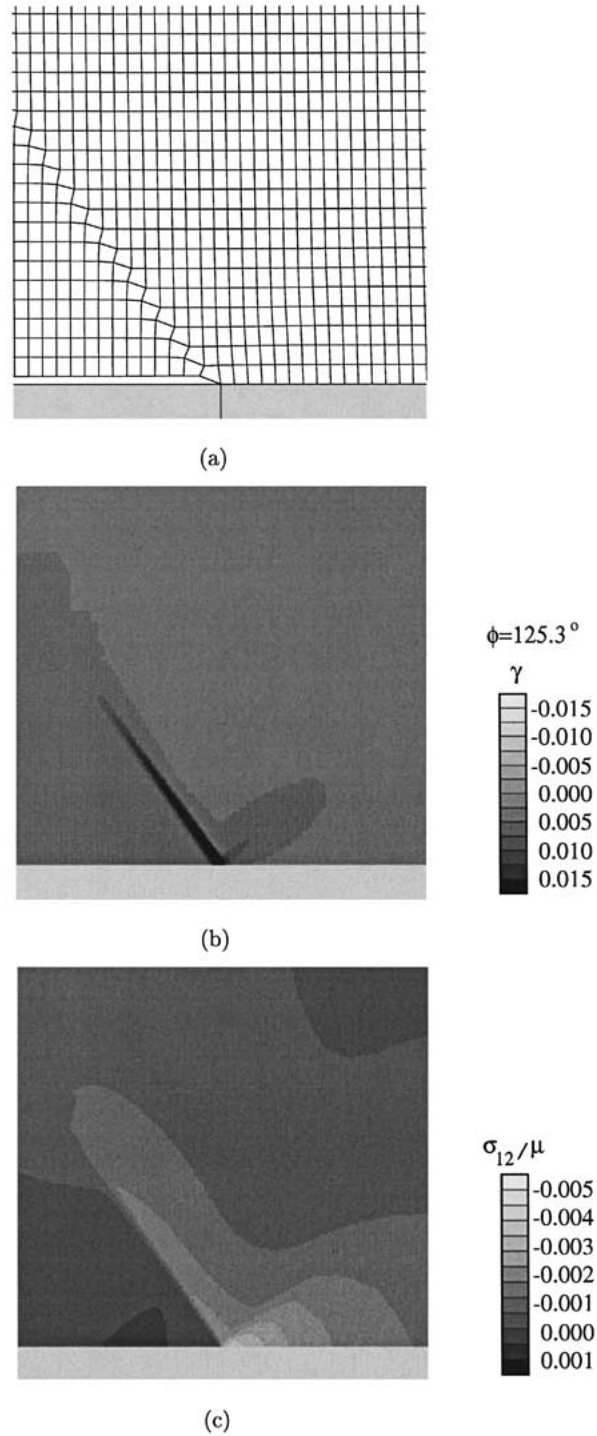


Figure 13. Continuum slip predictions for the two-slip-system fcc type crystal geometry at $K_1/K_0 = 0.717$. (a) Deformed mesh. The size of the region shown is $6 \times 6 \mu\text{m}$. (b) Slip distribution for $\phi^{(2)} = 125.3^\circ$. The size of the region shown is $24 \times 24 \mu\text{m}$. (c) Contours of σ_{12} . The size of the region shown is $24 \times 24 \mu\text{m}$.

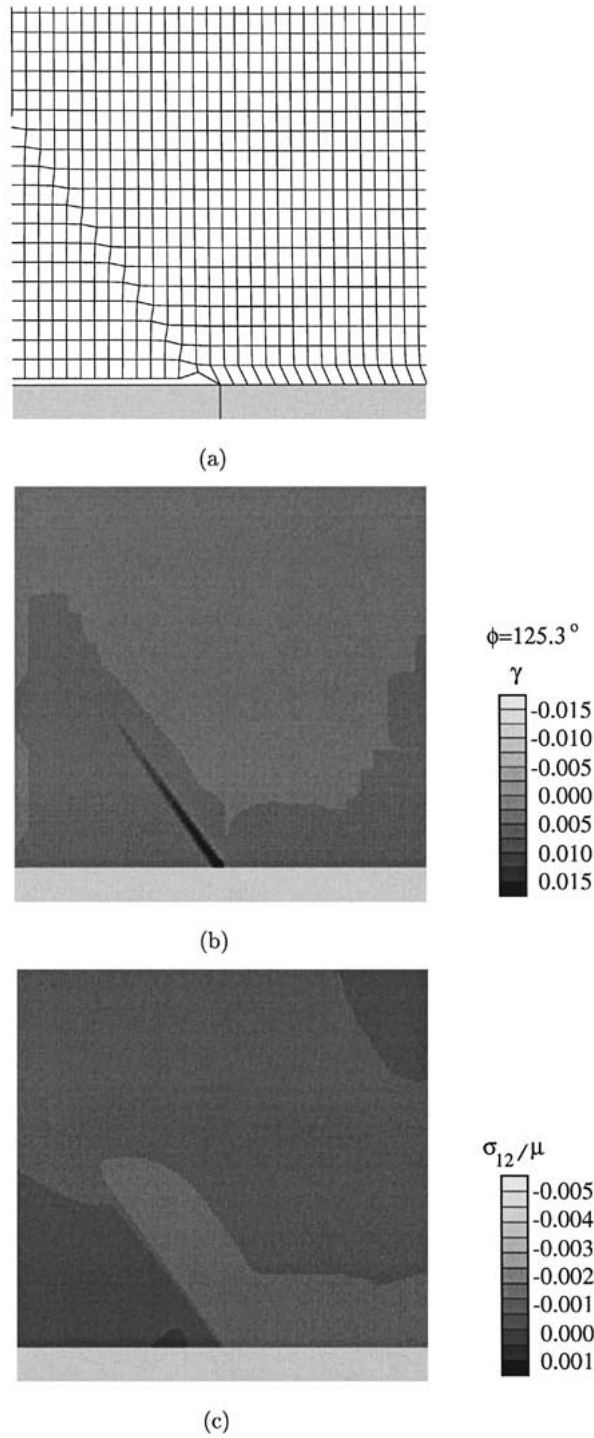


Figure 14. Continuum slip predictions for the three-slip-system fcc type crystal geometry at $K_1/K_0 = 0.717$. (a) Deformed mesh. The size of the region shown is $6 \times 6 \mu\text{m}$. (b) Slip distribution for $\phi^{(2)} = 125.3^\circ$. The size of the region shown is $24 \times 24 \mu\text{m}$. (c) Contours of σ_{12} . The size of the region shown is $24 \times 24 \mu\text{m}$.

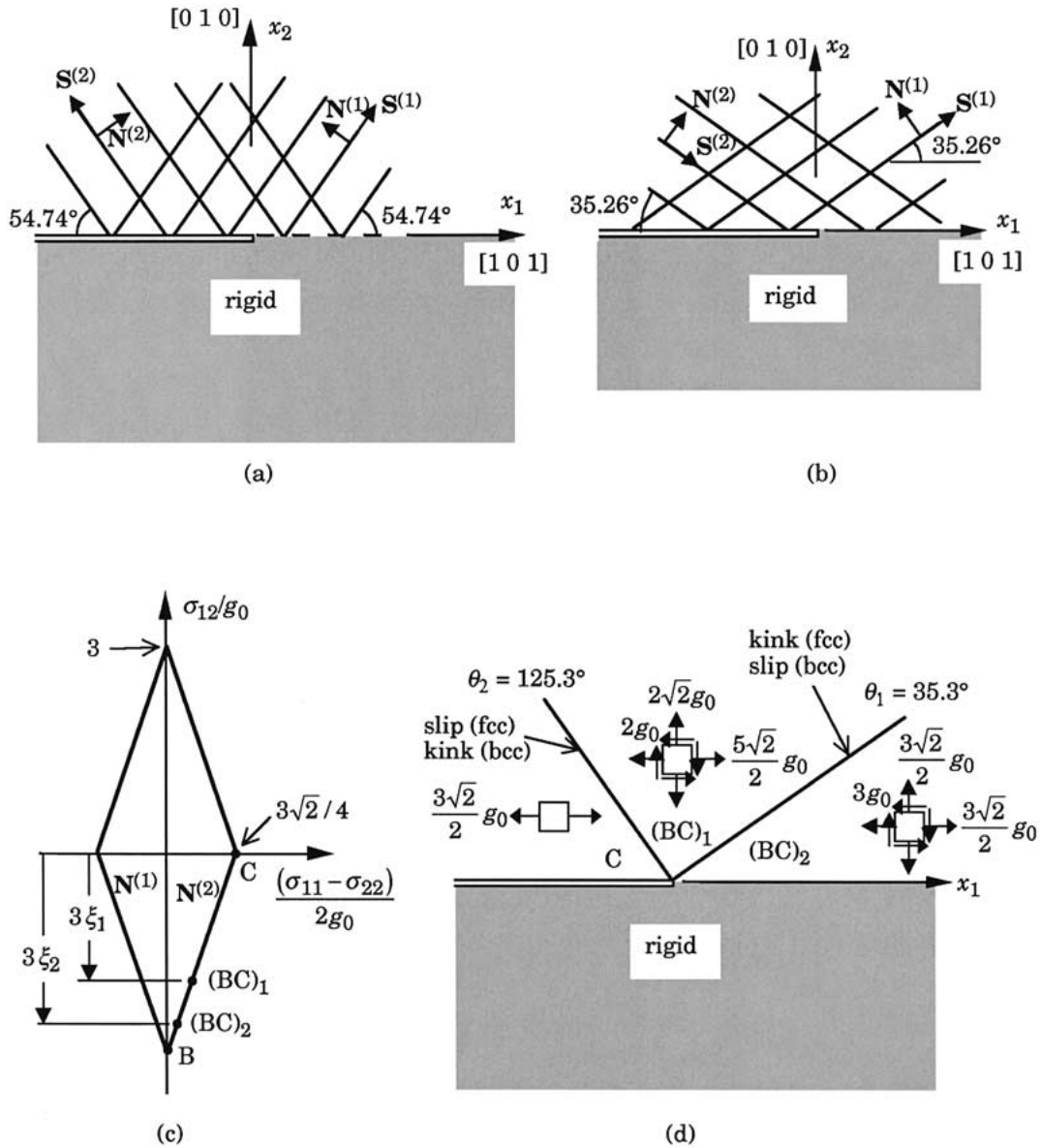


Figure 15. Interface crack between a two-slip-system crystal and a rigid substrate: (a) physical plane illustrating slip plane traces for the fcc type orientation; (b) physical plane for the bcc type orientation; (c) stress plane showing the yield surface with $\mathbf{N}^{(i)}$ illustrated for the fcc type orientation ($\mathbf{N}^{(1)}$ and $\mathbf{N}^{(3)}$ switch for the bcc type orientation); (d) asymptotic analytical solution for both the fcc type and the bcc type orientations that is in agreement with the discrete dislocation simulations and with the numerical continuum slip solutions ($\xi_1 = 2/3$, $\xi_2 = 1$).

with the sign convention used in (13) and (14). The associated yield surface in the stress plane is shown in Figure 15c and is diamond-shaped. The unit normal vectors $N_i^{(\alpha)}$ to the slip plane traces in the physical plane correspond to the straight-line portions of the yield surface labeled in the stress plane. Note that, consistent with the numerical analyses, we adopt identical yield surfaces for the fcc and bcc cases; as will be shown, this will result in the near-tip solutions being identical in these two cases when expressed in terms of the planar slip system flow strength g_0 (assumed equal on all planar slip systems) except that rays of stress and displacement discontinuity change from slip to kink type (or *vice-versa*) in going from fcc to bcc.

To construct an asymptotic solution, one observes that the stress plots in Figures 6 and 7 from the discrete dislocation results strongly suggest that the near-tip solution in both the fcc and bcc cases is comprised of three angular constant stress sectors. From Figures 15a and 15b it is seen that there are only four admissible locations for sector boundaries: $\theta = 35.3^\circ$, 54.7° , 125.3° and 144.7° , as measured counterclockwise from the x_1 -axis. These are the angular locations of permissible slip or kink-type discontinuities (see the unit normal vectors in Figures 15a, b); whether each of these angles corresponds to a discontinuity of slip or kink type depends on the angle and whether the case is fcc or bcc, as will be discussed. Perhaps the strongest evidence from the numerical simulations for which of these angles should constitute the sector boundary locations comes from the slip distribution results. For the fcc case, Figure 4 shows that there is a kink band located ahead of the crack tip, and what is primarily a slip band located behind the crack tip. Figure 15a shows that the only admissible location of a kink band ahead of the crack tip is at $\theta = 35.3^\circ$, and the only admissible location of a slip band behind the crack tip is at $\theta = 125.3^\circ$. Thus, the asymptotic fcc solution will be constructed with these locations as sector boundaries. Note that the results from the two-slip-system fcc continuum slip numerical simulation, Figure 13, are also supportive of such a three-sector solution with the boundary angles just noted.

For the bcc case, Figure 5 shows that there is a slip band located ahead of the crack tip, and what is primarily a kink band located behind the crack tip. Figure 15b shows that the only admissible location for a slip band ahead of the crack tip is at $\theta = 35.3^\circ$, and the only admissible location of a kink band behind the crack tip is at $\theta = 125.3^\circ$. Thus, the asymptotic bcc solution will be constructed with these locations as sector boundaries; note that these sector boundary locations are identical to those for the asymptotic fcc solution, but each has changed its slip/kink character, as shown in Figure 15d.

The yield surface plot from the numerical continuum slip solution, Figure 17a, which is identical for the fcc and bcc cases, also strongly implies a three-sector near-tip field having the boundary angles just noted, and provides perhaps the most definitive evidence from the numerical solutions on how such an asymptotic solution should be constructed.

An asymptotic analytical solution that is in accord with key features of the discrete dislocation simulations and with the numerical continuum slip solutions is shown in Figure 15d. We begin the analysis by recalling that we assume the stress state is at yield at all angles about the crack tip in the crystal. The stress state in this solution will be identical for the fcc and bcc cases when expressed in terms of the planar slip system flow strength g_0 , since we are using the same yield surface for both; only the character of the sector boundaries (slip or kink type) will differ. First, the constant stress sector adjacent to the crack flank must have $\sigma_{12} = \sigma_{22} = 0$ from the traction-free boundary condition on the crack face. The stress contours of σ_{11} in Figures 6c and 7c show that $\sigma_{11} > 0$ adjacent to the crack flank, as does the stress state evolution of Figure 17a. Together these indicate that the stress state in the sector

adjoining the crack flank is of type C, as indicated on the yield surface of Figure 15c. From this yield surface and the boundary conditions just noted, the stress state in sector C is

$$\frac{\sigma_{11} - \sigma_{22}}{2g_0} = \frac{3\sqrt{2}}{4}, \quad \frac{\sigma_{11} + \sigma_{22}}{2g_0} = \frac{3\sqrt{2}}{4}, \quad \frac{\sigma_{12}}{g_0} = 0. \quad (16)$$

This sector then adjoins a sector of type $(BC)_1$ via a radial stress jump along $\theta = 125.3^\circ$; movement from state C to state $(BC)_1$, which the asymptotic analysis permits to lie anywhere along the BC line on the yield surface in Figure 15c, corresponds to a slip-type (fcc) or kink-type (bcc) discontinuity across $\theta = 125.3^\circ$ as discussed above. Rice (1987) showed that the stress jump produced by traversing any part of a yield surface flat is given by

$$\llbracket \frac{1}{2}(\sigma_{11} + \sigma_{22}) \rrbracket = \pm \llbracket \ell \rrbracket, \quad (17)$$

where ℓ is arc length along the yield surface, having units of stress and increasing in the counterclockwise sense, $\llbracket f \rrbracket \equiv f(\theta^+) - f(\theta^-)$ and Drugan (2001) shows why the right side of (17) is in general preceded by \pm .

The sector averaged hydrostatic stress results from both the numerical continuum slip solution, Figure 19a, and the discrete dislocation analysis, Figure 20, show that the stress triaxiality increases as one progresses from sector C to sector $(BC)_1$. Using this in conjunction with (17), (16) and the yield surface of Figure 15c, the stress state in sector $(BC)_1$ is computed to be

$$\frac{\sigma_{11} - \sigma_{22}}{2g_0} = (1 - \xi_1) \frac{3\sqrt{2}}{4}, \quad \frac{\sigma_{11} + \sigma_{22}}{2g_0} = (1 + 3\xi_1) \frac{3\sqrt{2}}{4}, \quad \frac{\sigma_{12}}{g_0} = -3\xi_1, \quad (18)$$

where $0 < \xi_1 < 1$, and ξ_1 and ξ_2 are as defined in Figure 15c.

The numerical continuum slip solutions, Figure 19a, also show that the stress triaxiality decreases in going from sector $(BC)_1$ to the sector ahead of the crack tip. Yet, Figure 17a shows that the stress state continues to move along the BC yield surface flat toward $(BC)_2$. As Figures 15a and 15b show, movement along the BC flat of the yield surface can only occur either as a jump at $\theta = 125.3^\circ$, as in the sector C to $(BC)_1$ boundary, or along $\theta = 35.3^\circ$, the boundary location between sector $(BC)_1$ and sector $(BC)_2$. The stress state in sector $(BC)_2$ is free to lie anywhere along the BC segment between states $(BC)_1$ and B in Figure 15c. Using (16) and (18), its stress state is, with $0 < \xi_1 < \xi_2 \leq 1$:

$$\frac{\sigma_{11} - \sigma_{22}}{2g_0} = (1 - \xi_2) \frac{3\sqrt{2}}{4}, \quad \frac{\sigma_{11} + \sigma_{22}}{2g_0} = [1 + 3(2\xi_1 - \xi_2)] \frac{3\sqrt{2}}{4}, \quad \frac{\sigma_{12}}{g_0} = -3\xi_2. \quad (19)$$

Correct asymptotic solutions can be found for all ξ_1, ξ_2 values lying in the range $0 < \xi_1 < \xi_2 \leq 1$. From the stress plane plot in Figure 17a, it seems that the choice of these parameters that gives the best agreement between the analytical and numerical solutions at the highest loading level in Figure 17a is $\xi_1 \approx 2/3$ and $\xi_2 \approx 1$. The stress state illustrated in Figure 15d is for these values.

4.3.2. Three slip systems

The analysis for the fcc and bcc type crystal geometries having three slip systems is illustrated in Figure 16. In accordance with the numerical simulations, we have assumed an equal planar slip system flow strength of g_0 on all slip systems, for both the fcc and bcc cases. The yield surface is now hexagonal. Perhaps surprisingly, the asymptotic solution that agrees with the

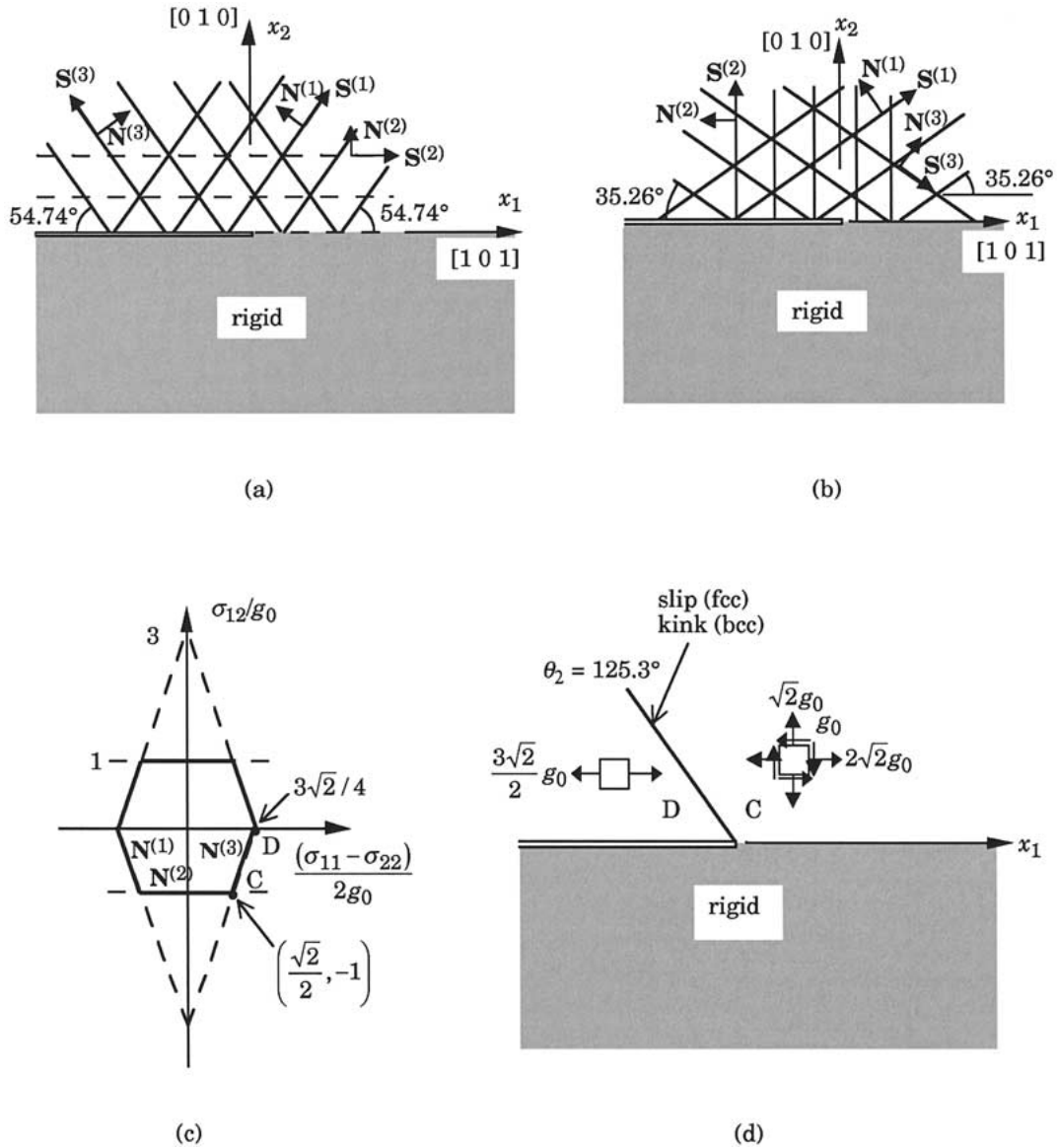


Figure 16. Interface crack between a three-slip-system crystal and a rigid substrate: (a) physical plane illustrating slip plane traces for the fcc type orientation; (b) physical plane for the bcc type orientation; (c) stress plane showing the yield surface with $\mathbf{N}^{(i)}$ illustrated for the fcc type orientation ($\mathbf{N}^{(1)}$ and $\mathbf{N}^{(2)}$ switch for the bcc type orientation); (d) asymptotic analytical solution for both the fcc type and bcc type orientations, in agreement with the discrete dislocation simulations and with the numerical continuum slip solutions.

three slip system discrete dislocation simulations is simpler than that for the two slip system crystals.

The discrete dislocation stress field results in Figures 10 and 12, especially the plots of σ_{12} and σ_{11} in Figure 10, and σ_{12} and σ_{22} in Figure 12, suggest an asymptotic solution with only two sectors. The contours of σ_{12} in Figure 14c, from the fcc numerical continuum slip solution for this case, also strongly suggests a two-sector asymptotic field, as do the results from the bcc solution.

For the fcc case, the slip distribution plots from the discrete dislocation simulation, Figure 9, show a single deformation band, which is primarily a slip band, located behind the crack tip. Figure 16a shows that the only admissible location for a slip band behind the crack tip is at $\theta = 125.3^\circ$. The discrete dislocation stress distributions in Figure 10, as well as the continuum slip results of Figure 14, strongly support this sector boundary location. For the bcc case, the slip distributions from the discrete dislocation simulation, Figure 11, are not as definitive as in the fcc case, but they appear to show a single predominant deformation band, which is primarily a kink band, emanating from the crack tip and located behind it. Figure 16b shows that the only admissible location for a kink band behind the crack tip in the bcc structure is at $\theta = 125.3^\circ$. The discrete dislocation stress contours in Figure 12 are not conclusive in this regard, but the σ_{22} plot in Figure 12b seems consistent with this boundary location. The numerical continuum slip results for the three-slip-system bcc crystal (not shown) support this boundary location.

The evolution of the sector averaged stress state from the numerical continuum slip solution, Figure 17, which is identical for the fcc and bcc cases, also strongly implies a two-sector near-tip field with the boundary location just proposed and provides perhaps the most definitive evidence from the numerical solutions on how such an asymptotic solution should be constructed.

An asymptotic analytical solution that is in accord with the discrete dislocation simulations and the numerical continuum slip solutions is shown in Figure 16d. As in the previous analyses, the traction-free crack face requirement demands $\sigma_{12} = \sigma_{22} = 0$ in the sector adjacent to the crack flank, and Figures 10c and 12c show that $\sigma_{11} > 0$ there, as does Figure 17b. Thus, the stress state in this sector corresponds to state D of the yield surface in Figure 16c. Next, we have argued that the solution should involve a slip-type (fcc) or kink-type (bcc) displacement discontinuity across $\theta = 125.3^\circ$. This is in accord with a stress jump from state D toward state C on the yield surface of Figure 16c. For $\theta < 125.3^\circ$, Figures 9a, c and 11b, c from the discrete dislocation simulations show slip on the two slip systems corresponding to vertex C on the yield surface of Figure 16c; also, Figure 17b shows that the stress state approaches vertex C at the higher loading levels. Thus, we conclude that the stress state in the second near-tip sector in Figure 16d corresponds to that of vertex C. Employing the traction-free crack face boundary conditions, the yield surface of Figure 16c, the stress jump relation (17) and assuming a stress triaxiality increase in going from Sector D to Sector C, as implied by the stress contours in Figures 10 and 12, and by the numerical continuum slip results in Figure 19b, we compute the following stress state for near the crack tip, illustrated in Figure 16d:

$$\text{Sector D : } \frac{\sigma_{11} - \sigma_{22}}{2g_0} = \frac{3\sqrt{2}}{4}, \quad \frac{\sigma_{11} + \sigma_{22}}{2g_0} = \frac{3\sqrt{2}}{4}, \quad \frac{\sigma_{12}}{g_0} = 0 \quad (20)$$

$$\text{Sector C : } \frac{\sigma_{11} - \sigma_{22}}{2g_0} = \frac{\sqrt{2}}{2}, \quad \frac{\sigma_{11} + \sigma_{22}}{2g_0} = \frac{3\sqrt{2}}{2}, \quad \frac{\sigma_{12}}{g_0} = -1. \quad (21)$$

5. Conclusions

The practically important problem of the stress and deformation fields near the tip of a crack lying along the interface joining a ductile single crystal to a nondeforming material has been analyzed. This has been accomplished by use of three different but complementary approaches:

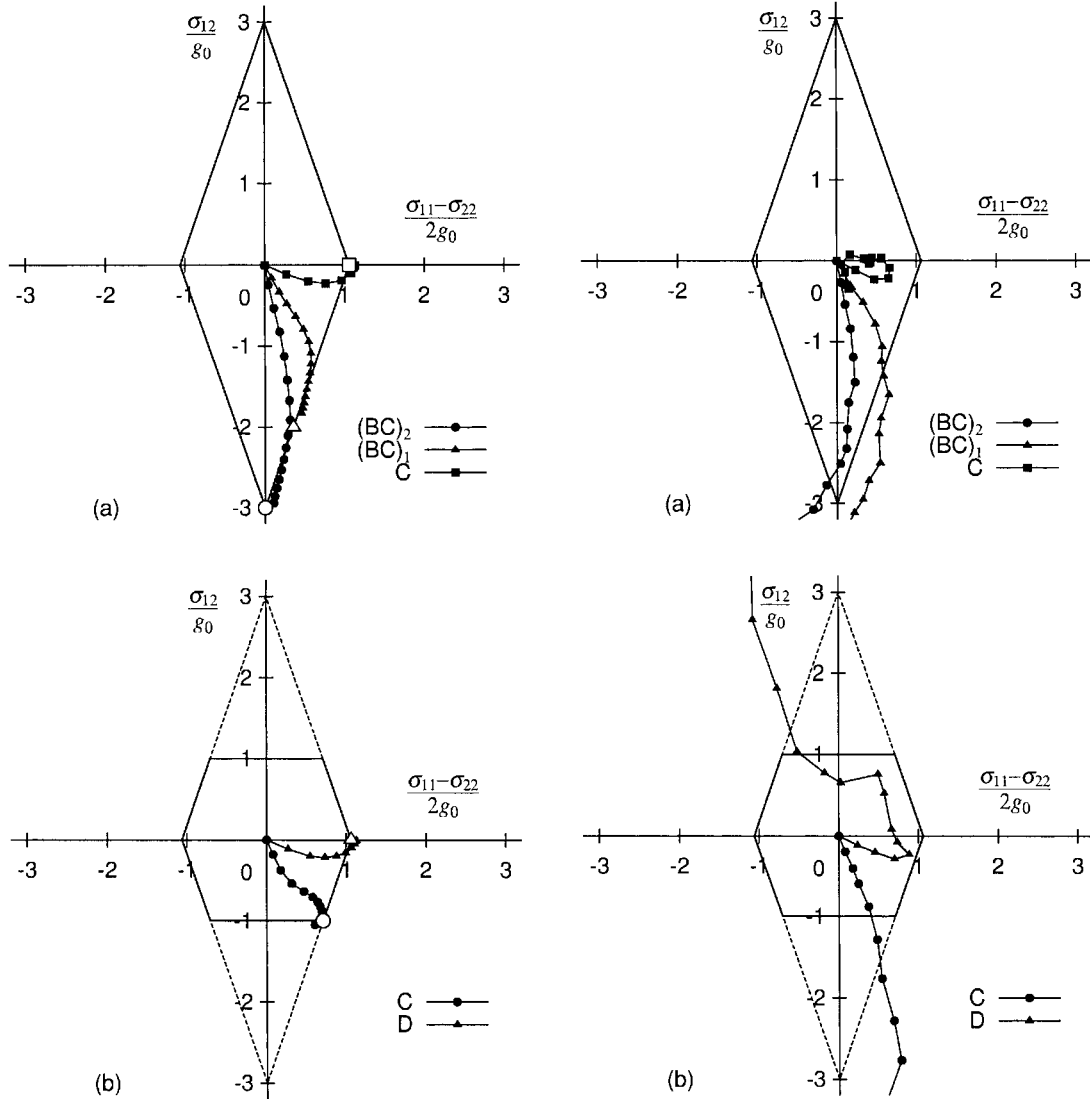


Figure 17. Evolution of the sector averaged stress state from the numerical continuum slip calculations. The averaging is carried out over an annular region centered at the crack tip with an inner radius of $0.5 \mu\text{m}$ and an outer radius of $1.5 \mu\text{m}$. (a) Two-slip-system fcc crystal with the sectors defined in Figure 15. (b) Three-slip-system fcc crystal with the sectors defined in Figure 16.

Figure 18. Evolution of the sector averaged stress state from the discrete dislocation calculations. The averaging is carried out over an annular region centered at the crack tip with an inner radius of $0.5 \mu\text{m}$ and an outer radius of $1.5 \mu\text{m}$. (a) Two-slip-system fcc crystal with the sectors defined in Figure 15. (b) Three-slip-system fcc crystal with the sectors defined in Figure 16.

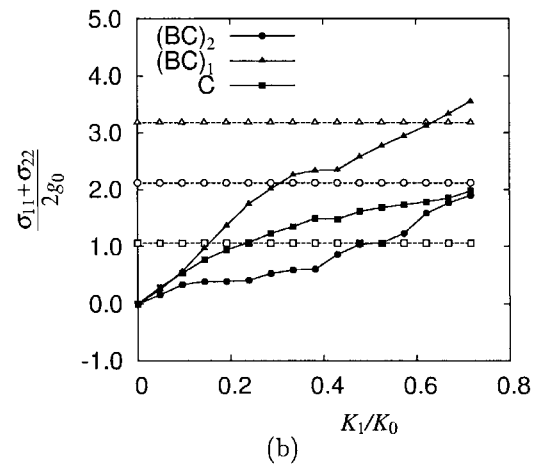
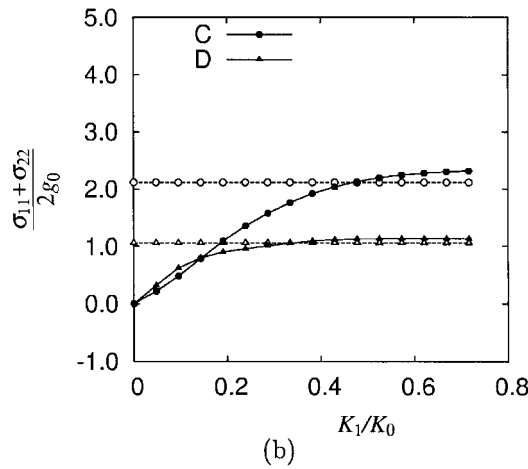
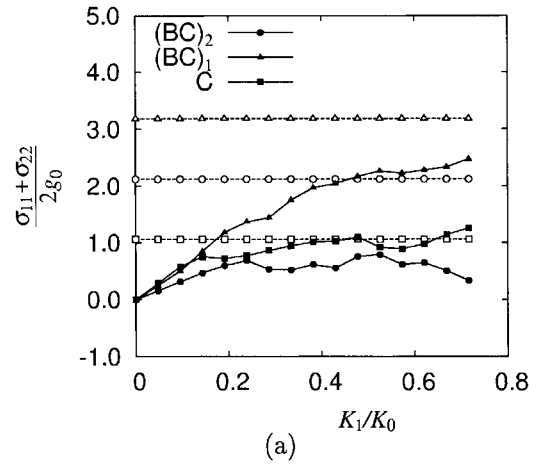
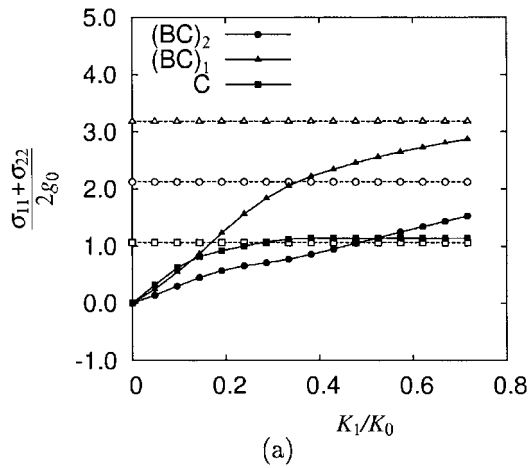


Figure 19. Comparison of the analytical (open symbols) and finite element (filled symbols) continuum slip solutions for the sector averaged values of $(\sigma_{11} + \sigma_{22})/g_0$. The sectors are defined in Figures 15 and 16. The averaging is carried out over an annular region centered at the crack tip with an inner radius of $0.5 \mu\text{m}$ and an outer radius of $1.5 \mu\text{m}$. The asymptotic continuum slip stress state is the same for the fcc type and bcc type orientations. (a) Two-slip-system fcc-type crystal. (b) Three-slip-system fcc-type crystal.

Figure 20. Comparison of the analytical continuum slip solution (open symbols) and discrete dislocation results (filled symbols) for the sector averaged values of $(\sigma_{11} + \sigma_{22})/g_0$. The sectors are defined in Figure 15. The averaging is carried out over an annular region centered at the crack tip with an inner radius of $0.5 \mu\text{m}$ and an outer radius of $1.5 \mu\text{m}$. (a) Two-slip-system fcc-type orientation. (b) Two-slip-system bcc-type orientation.

a discrete dislocation simulation, and finite element and asymptotic analytical solutions for continuum slip crystal plasticity. There are great benefits to this simultaneous three-pronged attack: each of the approaches employs different types of assumptions, so that points of agreement among results obtained from the three approaches serve as confirmation of the reasonableness of the assumptions made and of the correctness of the resulting solutions. Furthermore, each approach provides certain key features of the behavior that the other approaches either cannot provide or provide in a less useful form. For example, the discrete

dislocation simulations provide a valuable window into the actual micromechanics of how the near-tip plastic deformation develops, and what the actual underlying dislocation distribution is that corresponds to the macroscopic elastic-plastic deformation pattern. But limitations on how many dislocations can be handled and how many computer runs can be made, make it difficult to determine the near-tip stress and deformation fields that occur on a larger scale near such a crack tip. This information can be obtained from the numerical finite element continuum slip crystal plasticity solutions, which give full-field results for the elastic-plastic stress and deformation fields. Both numerical approaches also accurately show the crack tip opening behavior, which is important in understanding the type of failure anticipated. Despite this valuable information, the numerical approaches are necessarily limited in their precision. The advantages of the asymptotic analytical solutions are the provision of exact results for the continuum near crack tip fields, and rather simple closed-form analytical expressions for the near-tip stress fields and for key features of the corresponding deformation fields.

For a three-slip-system crystal, Figure 19b, the sector averaged stresses calculated from the numerical continuum slip plasticity solutions approach the analytical asymptotic solution. For a two-slip-system crystal, Figure 19a, the asymptotic stress state is not yet attained in the numerical solution, although the approach to the analytical asymptotic solution can be seen. Having assembled asymptotic analytical solutions consistent with the numerical solutions, the analytical solutions provide a framework for interpreting the structure embedded in the numerical results, both continuum slip and discrete dislocation. The numerical solutions, in turn, show the range of validity of the asymptotic analytical solutions, both close to the crack tip where discrete dislocation effects come into play and away from the crack tip where the asymptotic fields no longer are dominant.

Our results show that the addition of a third slip system to ductile single crystals having two slip systems has a significant effect on the interface crack-tip fields. Regarding the deformation fields, for both the two- and three-slip-system fcc type crystal geometries, the predominant feature of the crack deformation field is a strong slip band oriented at $\theta = 125.3^\circ$ from the line ahead of the crack, and this produces substantial blunting (opening) of the crack tip, more in the three-slip-system case than the two-slip-system one. Another difference between the two- and three-slip-system fcc type crystal geometries is the presence of an additional band of concentrated plastic shearing, of kink type, at $\theta = 35.3^\circ$ in the two-slip-system case that is not present in the three-slip-system case, although far less shearing occurs on this band than on the slip-type band.

The near-tip deformation field in the bcc crystals contains a band of concentrated plastic shearing of kink type at $\theta = 125.3^\circ$ in both the two- and three-slip-system bcc type crystal geometries, while the two-slip-system bcc type crystal geometry contains an additional band of concentrated plastic shearing of slip type at $\theta = 35.3^\circ$ (compare Figures 5b and 11b). In dramatic contrast to the fcc crystal geometries, these concentrated shearing bands do not produce significant crack tip opening. The deformation field features discussed in the present and previous paragraph are perhaps best illustrated in Figures 3 and 8a.

Another significant difference between the two- and three-slip-system crystal geometries is the degree of complexity of the continuum slip crack tip fields. In both the fcc and bcc cases, the near-crack-tip fields in the two-slip-system crystals are comprised of three different angular plastic sectors having constant Cartesian components of stress (with rays of concentrated plastic shearing along each of the two inter-sector boundaries and radial normal stress jumps across these boundaries), while the near-tip fields in the three-slip-system crystals are comprised of only two different angular plastic constant stress sectors (with a single ray of

concentrated plastic shearing along the inter-sector boundary, which is also the site of a radial normal stress jump). These differences are illustrated in Figures 15d and 16d.

Neither of the approaches based on a conventional continuum description of crystal plasticity can capture the localized high stresses that will be responsible for crack growth (Cleveringa et al., 2000). Moreover, very near the crack tip the slip patterns in Figures 9 and 11 involve slip on all three slip systems whereas the continuum plasticity solutions (see Figures 15 and 16) involve one or two slip systems. The significant differences between the near crack tip stress states obtained from the discrete dislocation and continuum slip analyses is seen by comparing Figures 17 and 18. Both these Figures show the stress state evolution in stress space for the two-slip-system and three-slip-system crystals with the fcc-like orientation in terms of sector averaged stresses. The near crack tip stress states obtained from the discrete dislocation analyses, Figure 18, exhibit some of the features seen in the continuum slip analyses, Figure 17, but the effect of the high local stresses associated with the near tip dislocation structures is evident. Figure 18 also shows that a change in stress path can be associated with the near crack tip discrete dislocation stress state, for example in Sector D in Figure 18b. In Figure 20, the discrete dislocation sector averaged stresses are compared with the analytical continuum slip predictions. In the discrete dislocation results there is a difference between the fcc- and bcc-type orientations, whereas the continuum slip stress fields coincide for these two orientations.

Acknowledgements

Support from the Materials Research Science and Engineering Center on *On Micro-and-Nano-Mechanics of Electronic and Structural Materials* at Brown University (NSF Grant DMR-0079964) is gratefully acknowledged. W.J. Drugan is also pleased to acknowledge support from Grant CMS-9800157 from the *Mechanics and Materials Program* of the U.S. National Science Foundation and A. Nakatani thanks the Ministry of Education, Science, Sports and Culture, Japan for the Overseas Research Fellowship granted.

References

- Asaro, R.J. (1983). Micromechanics of crystals and polycrystals. *Advances in Applied Mechanics* **23**, 1–115.
- Bassani, J.L. (1994). Plastic-flow of crystals. *Advances in Applied Mechanics* **30**, 191–258.
- Cleveringa, H.H.M., Van der Giessen, E. and Needleman, A. (2000). A discrete dislocation analysis of mode I crack growth. *Journal of the Mechanics and Physics of Solids* **48**, 1133–1157.
- Cuitiño, A.M. and Ortiz, M. (1993). Computational modelling of single crystals. *Modelling and Simulation in Materials Science and Engineering* **1**, 225–263.
- Deshpande, V.S., Needleman, A. and Van der Giessen, E. (2003). Discrete dislocation plasticity modeling of short cracks in single crystals. *Acta Materialia* **51**, 1–15.
- Drugan, W.J. (2001). Asymptotic solutions for crack tip fields without kink-type shear bands in elastic-ideally plastic single crystals. *Journal of the Mechanics and Physics of Solids* **49**, 2155–2176.
- Dundurs, J. (1969). Discussion of a paper by D.B. Bogy. *Journal of Applied Mechanics* **36**, 650–652.
- England, A.H. (1965). A crack between dissimilar media. *Journal of Applied Mechanics* **32**, 400–402.
- Erdogan, F. (1965). Stress distribution in bonded dissimilar materials with crack. *Journal of Applied Mechanics* **32**, 403–410.
- Hutchinson, J.W. and Suo, Z. (1992). Mixed-mode cracking in layered materials. *Advances in Applied Mechanics* **29**, 69–191.
- Rice, J.R. (1987). Tensile crack tip fields in elastic-ideally plastic crystals. *Mechanics of Materials* **6**, 317–335.

- Rice, J.R. (1988). Elastic fracture mechanics concepts for interfacial cracks. *Journal of Applied Mechanics* **55**, 98–103.
- Rice, J.R., Hawk, D.E. and Asaro, R.J. (1990). Crack tip fields in ductile crystals. *International Journal of Fracture* **42**, 301–321.
- Rice, J.R. and Sih, G.C. (1965). Plane problems of cracks in dissimilar materials. *Journal of Applied Mechanics* **32**, 418–423.
- Saeedvafa, M. and Rice, J.R. (1989). Crack tip singular fields in ductile crystals with Taylor power-law hardening. II: plane strain. *Journal of the Mechanics and Physics of Solids* **37**, 673–691.
- Shih, C.F. (1991). Cracks on bimaterial interfaces - elasticity and plasticity aspects. *Materials Science and Engineering* **A143**, 77–90.
- Van der Giessen, E., Deshpande, V.S., Cleveringa, H.H.M. and Needleman, A. (2001). Discrete dislocation plasticity and crack tip fields in single crystals. *Journal of the Mechanics and Physics of Solids* **49**, 2133–2153.
- Xu, X.-P. and Needleman, A. (1993). Void nucleation by inclusion debonding in a crystal matrix. *Modelling and Simulation in Materials Science and Engineering* **1**, 111–132.